Phys. Med. Biol. **43** (1998) 1001–1013. Printed in the UK PII: S0031-9155(98)90627-3

High-resolution 3D Bayesian image reconstruction using the microPET small-animal scanner

Jinyi Qi†, Richard M Leahy†§, Simon R Cherry‡, Arion Chatziioannou‡ and Thomas H Farquhar‡

† Signal and Image Processing Institute, University of Southern California, Los Angeles, CA 90089-2564, USA

‡ Imaging Sciences Division, Crump Institute for Biological Imaging, B2-086 CHS, UCLA School of Medicine, 10833 LeConte Avenue, Los Angeles, CA 90024-6948, USA

Received 31 July 1997

Abstract. A Bayesian method is described for reconstruction of high-resolution 3D images from the microPET small-animal scanner. Resolution recovery is achieved by explicitly modelling the depth dependent geometric sensitivity for each voxel in combination with an accurate detector response model that includes factors due to photon pair non-collinearity and inter-crystal scatter and penetration. To reduce storage and computational costs we use a factored matrix in which the detector response is modelled using a sinogram blurring kernel. Maximum *a posteriori* (MAP) images are reconstructed using this model in combination with a Poisson likelihood function and a Gibbs prior on the image. Reconstructions obtained from point source data using the accurate system model demonstrate a potential for near-isotropic FWHM resolution of approximately 1.2 mm at the center of the field of view compared with approximately 2 mm when using an analytic 3D reprojection (3DRP) method with a ramp filter. These results also show the ability of the accurate system model to compensate for resolution loss due to crystal penetration producing nearly constant radial FWHM resolution of 1 mm out to a 4 mm radius. Studies with a point source in a uniform cylinder indicate that as the resolution of the image is reduced to control noise propagation the resolution obtained using the accurate system model is superior to that obtained using 3DRP at matched background noise levels. Additional studies using pie phantoms with hot and cold cylinders of diameter 1–2.5 mm and ^{18}FDG animal studies appear to confirm this observation.

1. Introduction

MicroPET is a high-resolution PET scanner designed for imaging small laboratory animals (Cherry *et al* 1997). It consists of a ring of 30 position-sensitive scintillation detectors, each with an 8×8 array of 2 mm $\times$ 2 mm $\times$ 10 mm lutetium oxyorthosilicate (LSO) crystals coupled via optical fibres to a multi-channel photomultiplier tube. The detector ring diameter of microPET is 172 mm with an imaging field of view of 112 mm transaxially by 18 mm axially. The measured intrinsic detector pair resolution is 1.68 mm FWHM (full width at half maximum) and the reconstructed image resolution, as measured using the 3D reprojection method of Kinahan and Rogers (1989), is approximately 2.0 mm FWHM isotropically at the centre of the field of view. The scanner has no septa and operates exclusively in 3D

§ Corresponding author: Richard M Leahy, Signal and Image Processing Institute, 3740 McClintock Avenue, EEB400, University of Southern California, Los Angeles, CA 90089-2564, USA. E-mail address: leahy@sipi.usc.edu

0031-9155/98/041001+13$19.50

mode. Here we report on the development of a Bayesian reconstruction method for the scanner.

The majority of fully 3D PET studies are reconstructed using algorithms based on the analytic relationship between the source distribution and its sinograms (Colsher 1980, Kinahan and Rogers 1989, Defrise *et al* 1997). The resolution of these methods is limited by the implicit assumption that the data correspond to true line integrals through the unknown source distribution. In contrast, iterative reconstruction algorithms that are based on a statistical model are able to maximize resolution recovery by accurate modelling of the system response. Furthermore, these methods can optimize performance in low-count situations through explicit modelling of the statistical variability inherent in photon limited coincidence detection.

Iterative 3D reconstruction represents a daunting computational challenge due to the large number of lines of response (LORs) collected for each data set. Kinahan *et al* (1996) reduce the dimension of the data by pre-processing using Fourier rebinning before applying the OSEM algorithm. While this leads to substantial cost savings, Fourier rebinning again assumes that the data are measurements of line integrals so that the potential for resolution recovery is lost with this approach. Several other investigators have approached the problem using a combination of sparse matrix structures and in-plane and axial symmetries to reduce computation and storage requirements (Chen *et al* 1991, Johnson *et al* 1995, 1997, Ollinger and Goggin 1996, Terstegge *et al* 1996). These methods model the detection process using geometrical computations based either on the intersection of detection 'tubes' with each voxel (Ollinger and Goggin 1996) or on depth dependent geometric sensitivity calculations based on the solid angles subtended at the detectors by each voxel (Chen *et al* 1991, Terstegge *et al* 1996). Johnson *et al* (1995) also use a detection tube intersection model but include a shift-variant weighting to model detector response. Here we build on this work by using a depth dependent solid angle calculation in combination with a spatially variant detector response model. Using a factored matrix form, similar to that described for the 2D case by Mumcuoglu *et al* (1996b), we are able to include this more accurate model at little additional computational cost compared to models that do not include detector response.

Many of the statistically based 3D reconstruction methods are based on the EM (Chen *et al* 1991, Johnson *et al* 1995) or OSEM (Johnson *et al* 1997) algorithms. Both approaches can exhibit high-variance behaviour at high iteration numbers and are regularized through early termination of the algorithm or by subsequent smoothing of the reconstructed images. Here we use a MAP formulation in which the variance and resolution of the reconstruction are controlled through the regularizing influence of a prior. The MAP methods do not typically exhibit the instabilities at higher iterations encountered using EM and OSEM and hence the choice of stopping point is not critical once effective convergence has been reached. To compute the MAP solution, we use a 3D extension of the pre-conditioned conjugate gradient algorithm described by Mumcuoglu *et al* (1996a, b).

2. Factored system model

2.1. The detection probability matrix

The theory of 3D MAP image reconstruction is essentially the same as for the 2D problem, differing primarily in the specifics of the detection probability matrix, $\mathbf{P}$. Even for microPET, which is small compared to the latest generation of clinical 3D PET systems, the $\mathbf{P}$ matrix is huge as shown in table 1. Sparseness and sinogram symmetry properties can be used to reduce this size to more reasonable proportions as previously described by Johnson

et al (1995) and Chen *et al* (1991). Here we combine the use of these symmetries with the factored system matrix approach that we previously applied to 2D PET (Mumcuoglu *et al* 1996b) to develop an accurate system model for which forward and backward projection can be performed efficiently.

Table 1. 3D problem dimensions for the microPET system. The projection matrix sizes are based on using eight bits to store each element of $\mathbf{P}_{\text{geom}}$ as described in section 2.2.

Ring diameter, mm	172	Object size, mm	$100 \times 100 \times 18$
Detectors per ring	240	Object size, voxels	$128 \times 128 \times 24$
Number of rings	8	Voxel size, mm	0.75^3
Angles per sinogram	120	Full size of $\mathbf{P}$, Gbytes	280
Rays per angle	100	Storage size of $\mathbf{P}_{\text{geom}}$, Mbytes	16
Number of sinograms	64	Storage size of $\mathbf{P}_{\text{blur}}$, Mbytes	0.02
Projections per sinogram	12 000	Storage size of $\mathbf{P}_{\text{attn}}$ and $\mathbf{P}_{\text{eff}}$, Mbytes	1.4
Total projection rays	768 000	Total storage size of $\mathbf{P}$, Mbytes	18

The elements, p_{ij}, of the detection probability matrix $\mathbf{P} \in \mathbb{R}^{M \times N}$ denote the probability of detecting an emission from pixel site j, $j = 1, \ldots, N$, at detector pair i, $i = 1, \ldots, M$. In order to reduce the stored size of the $\mathbf{P}$ matrix, we factor it as follows:

$$\mathbf{P} = \mathbf{P}_{\text{det.sens}}\mathbf{P}_{\text{det.blur}}\mathbf{P}_{\text{attn}}\mathbf{P}_{\text{geom}}\mathbf{P}_{\text{positron}}. \tag{1}$$

Here $\mathbf{P}_{\text{attn}} \in \mathbb{R}^{M \times M}$ is a diagonal matrix containing the attenuation factors. Since there is currently no transmission source for the microPET system, we calculate these factors by re-projecting an estimate of the attenuation image obtained using the region of support estimated from a preliminary emission image and assuming a constant attenuation coefficient of 0.095 cm^{-1}. The diagonal detector normalization matrix $\mathbf{P}_{\text{det.sens}} \in \mathbb{R}^{M \times M}$ is measured using a uniform cylindrical source. The data presented here are all for ^{18}F studies in which positron range is sub-millimetre. We therefore ignore these effects and set $\mathbf{P}_{\text{positron}} \in \mathbb{R}^{N \times N}$ equal to the identity matrix. In future studies we will investigate the use of positron range blurring model for isotopes other than ^{18}F. Here we concentrate on the two novel aspects of our model, i.e. modelling of geometrical sensitivity in $\mathbf{P}_{\text{geom}}$ and sinogram blurring factors in $\mathbf{P}_{\text{det.blur}}$.

2.2. The geometric projection matrix

$\mathbf{P}_{\text{geom}} \in \mathbb{R}^{M \times N}$ is the geometric projection matrix with each element (i, j) equal to the probability that a photon pair produced in voxel j reaches the front faces of the detector pair i in the absence of attenuation and assuming perfect photon-pair collinearity. It is calculated from the solid angle spanned from the voxel j to the faces of the detector pair i. After rotating the coordinates, we approximate the 3D solid angle as a product of two angles as illustrated in figure 1. The two angles for each voxel are computed, with reference to the regions in figure 1, as follows:

$$\theta = \begin{cases} \angle d_{21} V d_{22} & \text{voxel in region I} \\ \pi - \angle d_{11} V d_{21} & \text{voxel in region II} \\ \angle d_{11} V d_{12} & \text{voxel in region III} \\ \pi - \angle d_{12} V d_{22} & \text{voxel in region IV} \end{cases} \tag{2}$$

where V denotes the position of the centre of each voxel. To improve the accuracy of this model, each voxel is divided into 64 subvoxels and the angle from the centre of each

subvoxel is computed. The final $p_{\text{geom}}(i, j)$ is then computed as the average

$$p_{\text{geom}}(i, j) = \frac{1}{64\pi^2} \sum_{k=1}^{64} \theta_{x'-y'}(k)\theta_{x'-z'}(k). \tag{3}$$

In figure 2, we show the variation in $p_{\text{geom}}(i, j)$ for voxels lying along the centre of a projection tube for a single detector pair. This figure shows significant depth dependent sensitivity for this particular LOR; however we note that these pixels contribute to adjacent LORs in such a way that the overall sensitivity to each voxel for each sinogram is approximately uniform.

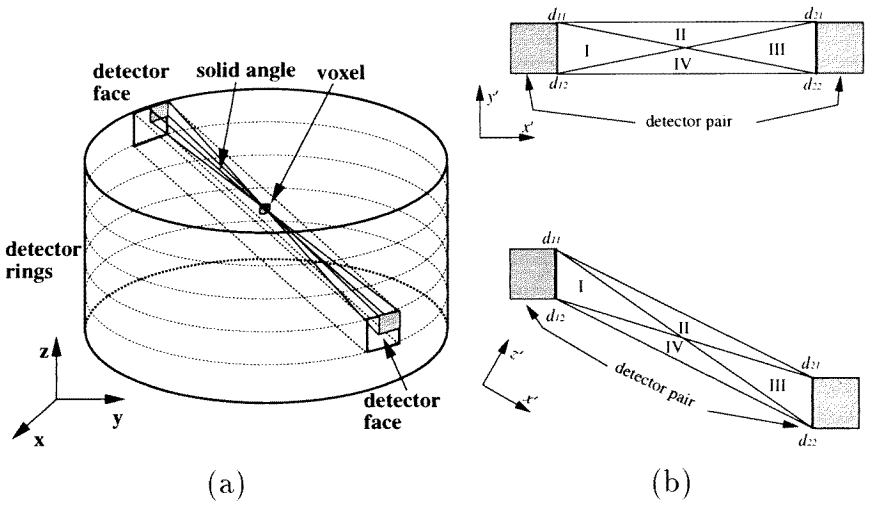

Figure 1. Geometry for computing $p_{\text{geom}}(i, j)$. The coordinates (x', y', z') are a rotation of the original coordinate first with respect to the z axis and then the y' axis, so that the x' axis is parallel to the line that joins the centres of two detector faces. (a) Illustration of the solid angle subtended at the detectors for a single voxel. (b) Cross sections in (x', y') and (x', z') planes.

$\mathbf{P}_{\text{geom}}$ is very sparse and has redundancies of which we can take advantage. By choosing the voxel size in the z direction to be an integer fraction of the ring distance, there are the following symmetries in the $\mathbf{P}_{\text{geom}}$ matrix (Johnson *et al* 1995, Chen *et al* 1991): in-plane rotation symmetries, resulting from rotating the projection rays by $\theta = 90^\circ, 180^\circ$ and 270°, and a $\theta = 45^\circ$ reflection symmetry. This provides a total factor of eight reduction. Axial reflection symmetry provides an additional factor of two reduction for ring differences other than zero. The parallel symmetry of sinograms with a common ring difference R_d provides a reduction by a factor of $(N_r - R_d)$ where N_r is the number of rings in the system. Combining these, the total reduction factor from the symmetry operations is approximately 64 for microPET. Therefore, we need only store the non-zero components of the base-symmetry LORs, which amount to 12440 LORs for microPET. Further savings in storage and computation can be realized by using an automated indexing scheme. This is achieved by storing a base pixel index and run length in the y direction for each value of x and z. By choosing the base symmetry lines of response so that they tend to run at small angles to the y direction, this scheme produces close to an additional factor of two saving in storage. Each element of the matrix is stored as a single eight-bit integer which is computed as $255 p_{\text{geom}}(i, j)/p_{\max}$. The constant $p_{\max}$ is the maximum solid angle in the

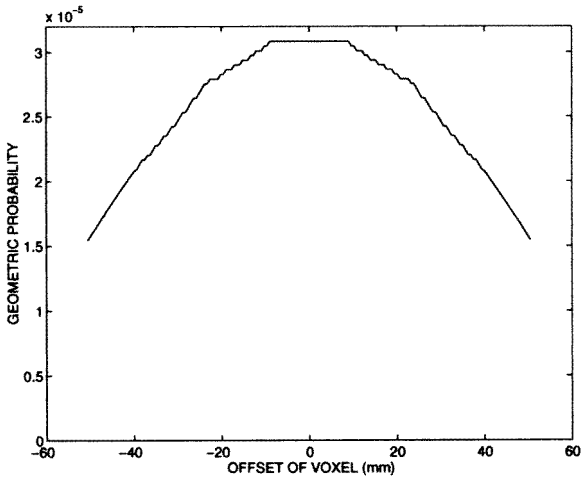

Figure 2. Values of $p_{\text{geom}}(i, j)$ for voxels lying along the centres of a detector tube for a single detector pair. The detector pair shown is at the centre of the field of view with a ring difference of zero. The field of view is 100 mm and the distance between the two detectors is 172 mm.

system computed at the point midway along the line joining the centres of the two detectors forming the shortest transaxial LOR.

2.3. The sinogram blurring matrix

$\mathbf{P}_{\text{blur}}$ is the sinogram blurring matrix used to model photon pair non-collinearity, inter-crystal scatter and penetration. In principle, uncertainties in the angular separation of the photon pair should be included in $\mathbf{P}_{\text{geom}}$; however, this will reduce its sparseness. We therefore lump this factor with the detector blurring effects by assuming that it is approximately depth independent. Similarly, we assume that the effects of inter-crystal scatter and detector penetration are independent of the distance of the positron annihilation point from the detectors.

In principle, a 3D sinogram blurring model should be used to model the radial, angular and inter-sinogram blurring. In our current implementation we have assumed that these blurring effects can be confined to a single sinogram and use a 2D blurring model. Furthermore, because the axial acceptance angle of microPET is small ($\leqslant 7.5^\circ$), we assume that the blurring kernels are identical for sinograms for all ring differences. We treat each crystal as a separate detector and therefore ignore effects associated with the location of each detector within the 8×8 blocks used in the microPET system. We then have a rotational symmetry in the blurring kernels due to rotational invariance of the detector geometry (Mumcuoglu *et al* 1996b). We note that although this model cannot account for variations in the blurring kernels that may occur due to block effects (e.g. photons scattered between a pair of adjacent detectors in two adjacent blocks will be modelled in the same way as scatter between adjacent pairs in the same block), the spatially variant sensitivity due to block structure is included in $\mathbf{P}_{\text{det.sens}}$. As a result of the rotational symmetry, we need only compute and store the blurring kernels for the projection rays for a single projection angle, which saves both computational time and storage size; the computational cost of performing the sinogram blurring is only a few per cent of that for computing the geometric projection. The blurring factors were computed using the Monte Carlo code described in (Mumcuoglu

et al 1996b). Statistical modelling of non-collinearity, crystal penetration and inter-crystal scatter in the LSO detectors was used to produce the blurring of the sinogram element under consideration into the neighbouring elements. Figure 3 shows the blurring kernels for two different LORs; note the significant crystal penetration for off-centre detector pairs due to the small crystal size.

To illustrate the size saving from factoring out the detector blur as compared to incorporating it in the geometric matrix, as is the case in Johnson *et al* (1995), we counted the number of nonzero elements in $\mathbf{P}_{\text{geom}}$ and in $\mathbf{P}_{\text{blur}}\mathbf{P}_{\text{geom}}$. To make the comparison fair, the resulting elements of $\mathbf{P}_{\text{blur}}\mathbf{P}_{\text{geom}}$ were quantized to the same number of levels as we use in $\mathbf{P}_{\text{geom}}$. Because of rotation symmetry, only the columns corresponding to the voxels in the plane $y = 0$ need to be counted. The number of nonzero elements corresponding to voxels with the same radial offset were averaged together in the z direction and the result is shown in figure 4. This shows a savings factor of approximately three from using the factored matrix. Further relative savings would be realized if a full 3D blurring model were used.

ray-1	0	ray+1	ray+2	ray+3	ray+4	ray+5
0	0	0	0	0	0.0016	0
0	0.0103	0.0028	0.0432	0.0056	0.0077	0.0019
0.0062	**0.1169**	0.1686	0.2459	0.0600	0.0140	0.0019
0.0063	0.0099	0.1711	0.0449	0.0604	0.0079	0.0018
0	0	0.0025	0	0.0052	0.0014	0.0022

(a)

ray-3	ray-2	ray-1	0	ray+1	ray+2	ray+3
0	0	0	0	0	0	0
0.0014	0.0092	0	0.0058	0	0.0081	0.0017
0	0.0055	0.0651	**0.6778**	0.0618	0.0060	0
0	0.0100	0.0658	0.0054	0.0630	0.0093	0
0.0018	0	0	0	0	0	0.0022

(b)

Figure 3. Sinogram blurring kernels for the sinogram components indicated by the bold characters corresponding to (a) the 20th and (b) the 50th out of 100 projection rays. These kernels are shown for the sinogram stored in interleaved format.

3. Image reconstruction

The factored system model described above was used in a statistical image reconstruction framework. The standard Poisson likelihood function was used for the data and a Gibbs prior with a Huber potential used to model the 3D image. The image was reconstructed by maximizing the log posterior density:

$$\hat{\boldsymbol{x}}(Y) = \arg\max_{\boldsymbol{x}} L(Y|\boldsymbol{x}) - \beta\phi(\boldsymbol{x}) \tag{4}$$

$$= \arg\max \sum_i [-\hat{Y}_i + Y_i \log(\hat{Y}_i)] - \beta \sum_j \sum_{\substack{k\in\mathcal{N}_j \\ k>j}} \kappa_{jk} V(x_j - x_k) \tag{5}$$

where Y are the measurements, β is the hyperparameter of the Gibbs prior and $\hat{Y}$ is the data associated with image $\boldsymbol{x}$, i.e. $\hat{Y} = \mathbf{P}\boldsymbol{x}$. We have not included scatter or randoms in this

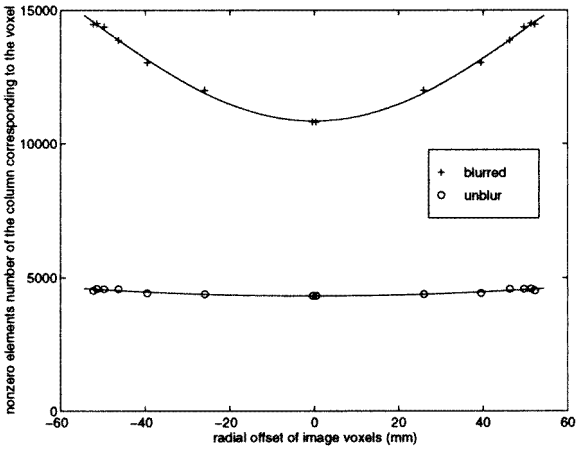

Figure 4. The average number of nonzero elements of different columns in $\mathbf{P}_{\text{geom}}$ and $\mathbf{P}_{\text{blur}}\mathbf{P}_{\text{geom}}$ corresponding to voxels at different radial offsets. The total numbers of nonzero elements in the two matrices were calculated using a radially weighted sum of the two curves to give an average ratio of 3:1 between $\mathbf{P}_{\text{blur}}\mathbf{P}_{\text{geom}}$ and $\mathbf{P}_{\text{geom}}$.

model. In small animals the total activity is small compared to that for human studies so that scatter and randoms fractions are much lower in the microPET system and are currently ignored in our work.

The Huber potential function $V(x_j - x_k)$ is

$$V(x_j - x_k) = \begin{cases} (1/2\delta_h)(x_j - x_k)^2 & \text{if } |x_j - x_k| \leqslant \delta_h \\ |x_j - x_k| - \dfrac{\delta_h}{2} & \text{otherwise} \end{cases} \tag{6}$$

where δ_h is a small constant. In the results presented below, δ_h was chosen to be very small, i.e. 1% or less of the maximum reconstructed image intensity. The neighbourhood $\mathcal{N}_j$ we used here is the second-order (26-voxel) neighbourhood with κ_{jk} equal to the reciprocal of the distance between the two voxels.

Using the factored matrix approach we gain substantial savings in storage and computational requirements. To fully realize this saving we must consider all data and all pixels at each iteration. Therefore the preconditioned conjugate gradient (PCG) approach (Mumcuoglu *et al* 1996a) and EM algorithms are more suitable for 3D reconstruction than either coordinate-wise methods (Bouman and Sauer 1996, Fessler 1994, Sauer and Bouman 1993) or ordered subset methods (Browne and De Pierro 1996, Hudson and Larkin 1994). In the case of coordinate-wise ascent, one complete iteration through the image will require the re-application of the blurring kernels each time a different pixel forward projects to a particular sinogram element; this results in substantial increases in computation cost. In the case of the ordered subset methods, efficiency is lost due to coupling of sinogram elements through the blurring kernels. Thus computation of the sinogram subset associated with the current image estimate requires forward projection into sinogram elements neighbouring the current subset. However, by approximating the blurring kernels as a 1D radial-only blurring function, we can use OSEM with the factored system model without loss in computational efficiency.

In all of the results shown below we used 20 iterations of the PCG method since the images were observed to change very slowly beyond this point. The procedure was

initialized using a constant image scaled so that the total counts resulting from forward projection of this image were equal to the total observed counts. For comparative purposes, we have shown images reconstructed using the 3D reprojection (3DRP) method of Kinahan and Rogers (1989). While it may also be possible to improve the performance of the 3DRP method by pre-filtering the data to compensate for the detector response (Huesman *et al* 1989, Liang 1994) or using a Wiener filter based approach (Shao *et al* 1994, Fessler 1994), these methods have not yet been widely studied in the 3D literature. In contrast, the standard 3DRP method used here serves as something of a gold standard in fully 3D reconstruction.

The computational cost of one iteration of the PCG algorithm is about 3 min on a 167 MHz Ultrasparc processor. Therefore, a $24 \times 128 \times 128$ voxel image requiring 20 iterations can be reconstructed within 60 min and a $24 \times 64 \times 64$ voxel image within 25 min. For comparison, the 3DRP method we used takes 15 minutes to reconstruct a $15 \times 128 \times 128$ voxel image, although we note that this program was not optimized.

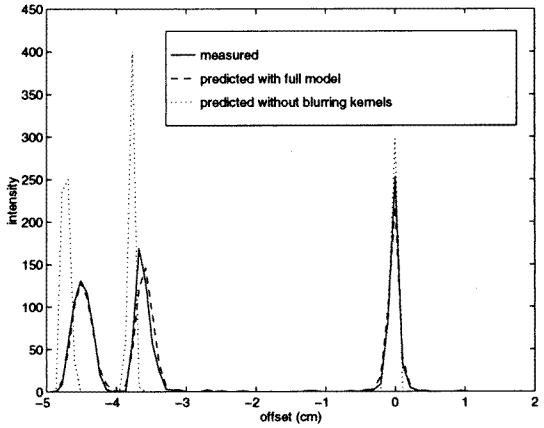

Figure 5. Profiles of the measured and calculated sinograms for the point source at different positions in the field of view.

4. Experimental results

4.1. Point source measurements

Our factored system model was tested using experimental measurements of a point source. A 0.5 mm diameter, 0.5 mCi ^{22}Na point source was scanned at different positions in the field of view. Each data set contained approximately 0.2 M total counts. We first compared the sinogram profile measured with that predicted using the factored system model. The results are shown in figure 5, with and without the inclusion of $\mathbf{P}_{\text{blur}}$. The figure shows that by using the blurring kernels, the asymmetry and peak shift due to crystal penetration are successfully followed. However, as we show below, errors in these blurring factors appear to be at least partially responsible for artifacts in the pie phantom studies. We are currently improving the Monte Carlo model of the detectors to correct this problem.

The point source data were reconstructed to investigate the potential for resolution recovery using our factored system model. The Poisson likelihood with positivity constraint can create artificially high resolution for a point source in zero background; resolution was therefore measured instead using a quadratically penalized weighted least-squares (PWLS)

method (Fessler 1994) without a positivity constraint. Profiles were taken through the point source images and the resolution determined by measuring the FWHM. Figure 6 shows plots of the radial and tangential components of the transaxial resolution, and also the axial resolution, compared to results obtained using the 3D reprojection method with a ramp filter with cut-off at the Nyquist frequency, i.e. half of the spatial sampling frequency for the interleaved sinogram. These clearly show that improvements in resolution can be achieved by using the accurate system model when compared to reconstruction obtained using either a simplified system model (no detector response modelling) or the 3DRP method with a ramp filter. The most dramatic improvement in resolution from the use of the blurring kernels occurs in the radial direction where we see a resolution of approximately 1 mm FWHM out to a 4 cm radius. The axial resolution is not improved by the 2D blurring kernels because we do not currently model axial blur. Some caution is necessary in interpreting these results. The FWHM resolution does not reflect the behaviour of the point spread functions (PSFs) below the half-maximum level and in fact in some locations we noted some lengthening of the tails of the PSF. Furthermore the estimators that we are using are nonlinear in the data so that resolution of point sources does not extrapolate directly to more distributed sources.

These point studies illustrate the potential gain that can be realized by accurately modelling the data. However, this gain is only useful if it can be achieved without large levels of noise amplification. We therefore also studied the trade-off between background noise levels and resolution using a point source in a uniform background. It is not possible to collect data for the point source in a uniform background because the point source is encased in a plastic sphere. Instead, we collected data from a uniform cylinder and added to this a separately acquired point source data set. By positioning the point source and the uniform cylinder at the centre of the field of view, the attenuation that would have occurred if the point source were actually inside the uniform cylinder would be constant along each LOR passing through the point source. Consequently, the combined data set should be virtually identical to that which would have been collected from a point source in a uniform background. We reconstructed images from the combined data set using the MAP method with different values of the hyperparameter β and the 3DRP method with a ramp filter with different cut-off frequencies. Figure 7 shows the resulting contrast recovery–background variance plots for the two methods. These plots show that at matched noise levels we can achieve superior contrast using the MAP method with the factored system model than when using 3DRP.

4.2. Hot- and cold-phantom studies

Specially constructed hot and cold pie phantoms were also scanned and reconstructed as shown in figure 8. These images show overall improvements in contrast in the MAP images compared to 3DRP and again we see little degradation in performance as the phantom is moved towards the edge of the field of view when using the factored matrix model. There are some differences in the MAP results between the centred and off-centred phantoms due to the small voxels (0.4 mm $\times$ 0.4 mm) used for the centred phantom compared to the larger voxel size (0.85 mm $\times$ 0.85 mm) for the off-centred phantom. The different sizes were used because the projection matrix for the small voxels becomes huge for the large field of view required for the off-centred phantom—note that the symmetries that are used to efficiently store the matrix preclude computing and storing the projection matrix for a small off-centred source region. The dark area at the top of the centred cold-spot phantom is due to an accumulation of air bubbles.

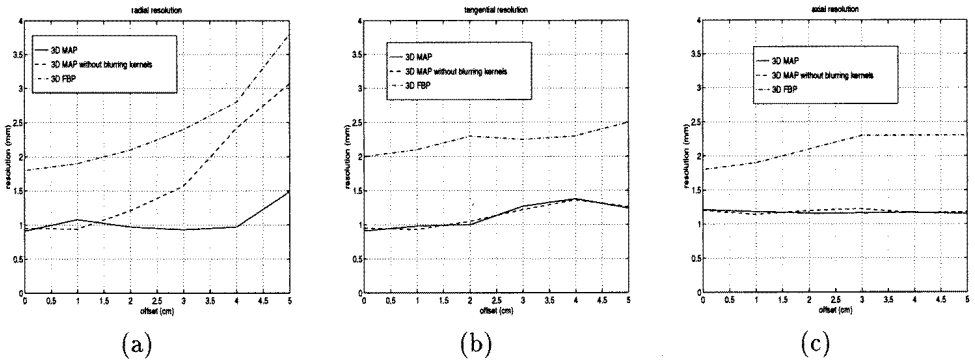

Figure 6. FWHM resolution of the point source image using 3DRP and PWLS, with and without modelling of the sinogram blur: (a) radial resolution, (b) tangential resolution, (c) axial resolution.

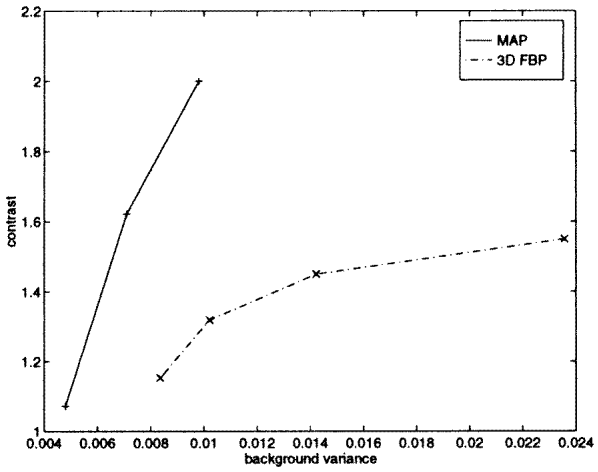

Figure 7. Contrast recovery for the point source against spatial variance of the cylinder for different smoothing parameters for the MAP and 3DRP methods.

There is a noticeable ring artifact at the edge of the cold phantom. The amplitude of this artifact is reduced when the MAP method is applied to simulated data, indicating that it is, in part, due to errors in the blurring kernels. However, the fact that the artifact remains when applied to simulated data and when using different iterative reconstruction methods (OSEM, least squares and penalized weighted least squares) is an indication that artifacts also arise from ill conditioning in the accurate system model. The ill conditioning gives rise to a Gibbs-like oscillation in the vicinity of sharp boundaries which are particularly prominent for near-circularly-symmetric objects such as the cold-spot phantom. Similar effects have been reported elsewhere (e.g. Snyder *et al* 1987). The artifact can be reduced or eliminated by increasing the degree of smoothing, but this will be at the expense of an overall loss in resolution.

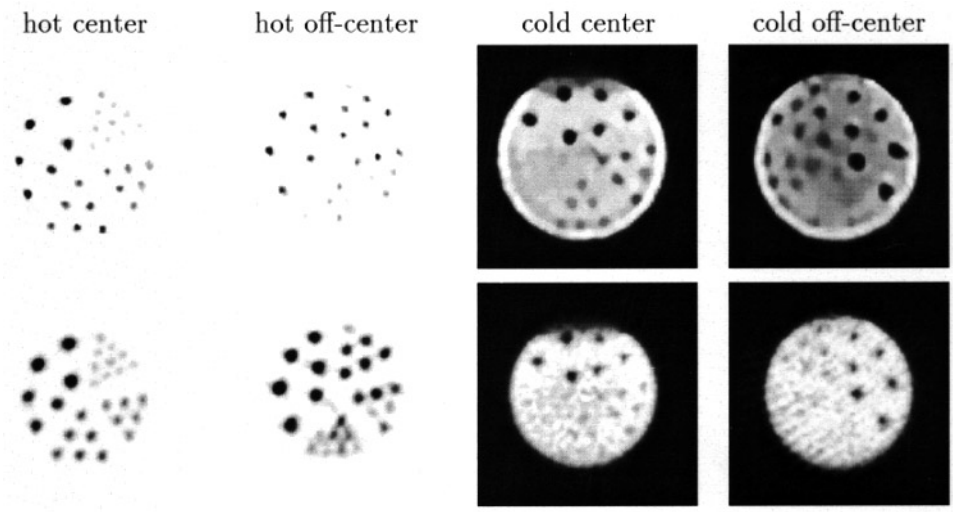

Figure 8. Reconstructions of hot and cold resolution phantoms at the centre and edge of the field of view with cylindrical regions of sizes 1.0, 1.25, 1.5, 2.0, 2.5 mm diameter. Top row: MAP reconstructions; Bottom row: 3DRP reconstructions. Hot phantom: ∼32 M total counts; cold phantom: ∼100 M total counts. The phantom occupied the entire axial field of view.

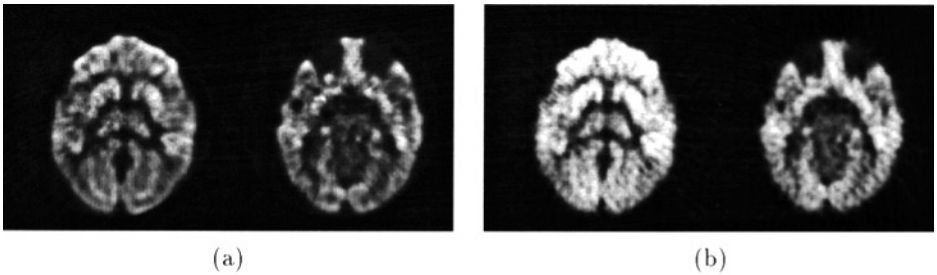

Figure 9. Baby monkey brain images reconstructed using (a) the 3D MAP method with full system model ($\beta = 2 \times 10^{-6}$); (b) the 3D reprojection method with ramp filter (cut-off frequency = 0.8 Nyquist frequency).

4.3. Animal studies

^{18}FDG data were collected from a 3 month old baby vervet monkey scanned using the microPET scanner after injection of 2.2 mCi of FDG. The total counts were about 64 M total counts for a collection time of 40 min. Figure 9 shows the image reconstructed by the 3D MAP method in comparison to the 3D reprojection method. The reconstructed field of view in these figures is a circle of diameter 8 cm with the maximum diameter of the brain approximately 6 cm. These images appear to confirm the resolution enhancement observed in the point source and pie phantom studies. The oblique stripes in the 3DRP reconstructions are probably due to imperfect detector normalization caused by time varying sensitivities. However, these artifacts are not seen in MAP reconstruction indicating a potential robustness of MAP to small errors in normalization factors.

5. Conclusions

We have described a fully 3D MAP reconstruction method for the high-resolution microPET animal scanner. We have shown that we can model and deconvolve the system response within this framework to achieve uniform transaxial resolution of 1 mm FWHM for objects up to a 4 cm diameter, and a resolution of about 1.2 mm up to an 8 cm diameter. These values reflect the maximum achievable resolution; when using noisy data, some loss in resolution is produced by increasing the hyperparameter β to control noise propagation. However, uniform cylinder plus point source studies show that the MAP method can achieve higher resolution than the 3D reprojection method at matched noise levels. These observations are also confirmed by the hot- and cold-spot phantom studies. The appearance of ring artifacts in the cylindrical cold-spot phantom indicates that the improvement in resolution is gained at the expense of increased ill conditioning in the system which results in increased sensitivity to modelling and numerical errors as well as noise. These artifacts can be reduced or suppressed by increasing the hyerparameter β but at the expense of reduced resolution.

Through optimization of storage and computational costs, reasonable reconstruction times can be achieved which should allow the routine use of this method in research studies. The methodology described here is also directly extendible to 3D human PET scanners.

Acknowledgment

This work was supported by the National Cancer Institute under grants No R01 CA579794 and No R01 CA69370.

References

Bouman C and Sauer K 1996 A unified approach to statistical tomography using coordinate descent optimization *IEEE Trans. Image Process.* **5** 480–92

Browne J and De Pierro A R 1996 A row-action alternative to the EM algorithm for maximizing likelihoods in emission tomography *IEEE Trans. Med. Imaging* **15** 687–99

Chen C, Lee S and Cho Z 1991 Parallelization of the EM algorithm for 3D PET image reconstruction *IEEE Trans. Med. Imaging* **110** 513–22

Cherry S R *et al* 1997 MicroPET: a high resolution PET scanner for imaging small animals *IEEE Trans. Nucl. Sci.* **44** 1161–6

Colsher J 1980 Fully three-dimensional positron emission tomography *Phys. Med. Biol.* **25** 103–15

Defrise M, Kinahan P E, Townsend D W, Michel C, Sibomana M and Newport D F 1997 Exact and approximate rebinning algorithms for 3-D PET data *IEEE Trans. Med. Imaging* **16** 145–58

Fessler J 1994 Penalized weighted least-squares image reconstruction for PET *IEEE Tran. Med. Imaging* **13** 290–300

Hudson H M and Larkin R S 1994 Accelerated image reconstruction using ordered subsets of projection data *IEEE Trans. Med. Imaging* **13** 601–9

Huesman R, Salmeron E and Baker J 1989 Compensation for crystal penetration in high resolution positron tomography *IEEE Trans. Nucl. Sci.* **36** 1100–7

Johnson C A, Seidel J, Carson R E, Gandler W R, Sofer A, Green M and Daube-Witherspoon M E 1997 Evaluation of 3D reconstruction algorithms for a small animal PET camera *IEEE Trans. Nucl. Sci.* **44** 1303–8

Johnson C, Yan Y, Carson R, Martino R and Daube-Witherspoon M 1995 A system for the 3D reconstruction of retracted-septa PET data using the EM algorithm *IEEE Trans. Nucl. Sci.* **42** 1223–7

Kinahan P, Michel C and Defrise M 1996 Fast iterative image reconstruction of 3D PET data *Proc. IEEE Nuclear Science Symp. and Medical Imaging Conf. (Anaheim, CA, 1996)* ed A Del Guerra (Piscataway, NJ: IEEE) pp 1918–22

Kinahan P and Rogers J 1989 Analytic 3D image reconstruction using all dectected events *IEEE Trans. Nucl. Sci.* **36** 964–8

Liang Z 1994 Detector response restoration in image reconstruction of high resolution positron emission tomography *IEEE Trans. Med. Imaging* **10** 314–21

Mumcuoglu E, Leahy R and Cherry S 1996a Bayesian reconstruction of PET images: methodology and performance analysis *Phys. Med. Biol.* **41** 1777–1807

Mumcuoglu E, Leahy R, Cherry S and Hoffman E 1996b Accurate geometric and physical response modeling for statistical image reconstruction in high resolution PET *Proc. IEEE Nuclear Science Symp. and Medical Imaging Conf. (Anaheim, CA, 1996)* ed A Del Guerra (Piscataway, NJ: IEEE) pp 1569–74

Ollinger J M and Goggin A S 1996 Maximum likelihood reconstruction in fully 3D PET via the SAGE algorithm *Proc. IEEE Nuclear Science Symp. and Medical Imaging Conf. (Anaheim, CA, 1996)* ed A Del Guerra (Piscataway, NJ: IEEE) pp 1594–8

Sauer K and Bouman C 1993 A local update strategy for iterative reconstruction from projections *IEEE Trans. Signal Process.* **41** 534–48

Shao L, Karp J and Countryman P 1994 Practical considerations of the Wiener filtering technique on projection data for PET *IEEE Trans. Nucl. Sci.* **41** 1560–5

Snyder D, Miller M, Thomas L and Politte D 1987 Noise and edge artifacts in maximum-likelihood reconstructions from emission tomography *IEEE Trans. Med. Imaging* **6** 228–38

Terstegge A, Weber S, Herzog H, Muller-Gartner H W and Hailling H 1996 High resolution and better quantification by tube of response modelling in 3D PET reconstruction *Proc. IEEE Nuclear Science Symp. and Medical Imaging Conf. (Anaheim, CA, 1996)* ed A Del Guerra (Piscataway, NJ: IEEE) pp 1603–7